



Tensor-cut: A tensor-based graph-cut blood vessel segmentation method and its application to renal artery segmentation

Chenglong Wang^{a,*}, Masahiro Oda^b, Yuichiro Hayashi^b, Yasushi Yoshino^c,
Tokunori Yamamoto^c, Alejandro F. Frangi^d, Kensaku Mori^{b,e}

^a Graduate School of Information Science, Nagoya University, Nagoya, Japan

^b Graduate School of Informatics, Nagoya University, Nagoya, Japan

^c Nagoya University Graduate School of Medicine, Nagoya, Japan

^d CISTIB Centre for Computational Imaging & Simulation Technologies in Biomedicine, School of Computing and School of Medicine, University of Leeds, United Kingdom

^e Research Center for Medical Bigdata, National Institute of Informatics, Japan



ARTICLE INFO

Article history:

Received 21 February 2019

Revised 18 November 2019

Accepted 25 November 2019

Available online 1 December 2019

Keywords:

Blood vessel segmentation

Graph-cut

Renal artery

Tensor

Hessian matrix

Riemannian manifold

ABSTRACT

Blood vessel segmentation plays a fundamental role in many computer-aided diagnosis (CAD) systems, such as coronary artery stenosis quantification, cerebral aneurysm quantification, and retinal vascular tree analysis. Fine blood vessel segmentation can help build a more accurate computer-aided diagnosis system and help physicians gain a better understanding of vascular structures. The purpose of this article is to develop a blood vessel segmentation method that can improve segmentation accuracy in tiny blood vessels. In this work, we propose a tensor-based graph-cut method for blood vessel segmentation. With our method, each voxel can be modeled by a second-order tensor, allowing the capture of the intensity information and the geometric information for building a more accurate model for blood vessel segmentation. We compared our proposed method's accuracy to several state-of-the-art blood vessel segmentation algorithms and performed experiments on both simulated and clinical CT datasets. Both experiments showed that our method achieved better state-of-the-art results than the competing techniques. The mean centerline overlap ratio of our proposed method is 84% on clinical CT data. Our proposed blood vessel segmentation method outperformed other state-of-the-art methods by 10% on clinical CT data. Tiny blood vessels in clinical CT data with a 1-mm radius can be extracted using the proposed technique. The experiments on a clinical dataset showed that the proposed method significantly improved the segmentation accuracy in tiny blood vessels.

© 2019 Elsevier B.V. All rights reserved.

1. Introduction

Blood vessel segmentation plays a fundamental role in many computer-aided diagnosis (CAD) systems, such as coronary artery stenosis quantification, cerebral aneurysm quantification, retinal vascular tree analysis, etc. This study focuses on the renal artery segmentation problem. Segmental renal artery clamping is a promising method to suppress warm ischaemic injury during partial nephrectomy (PN) (Shao et al., 2012, 2011; Yoshino et al., 2015). The segmentation of renal arteries helps physicians obtain a better understanding of vascular topology and allows further quantitative

analyses. However, renal artery segmentation remains difficult due to its low contrast and the kidney's complex internal structures, especially for tiny structures under a radius of 3 mm (about the 4th generation of dichotomous branching that extends from the abdominal aorta). No segmentation method exists that is designed for precise renal artery segmentation problems.

Due to low contrast and tiny elongated structures, accurate blood vessel segmentation remains an elusive challenge in many medical image-processing applications. Numerous blood vessel segmentation methods have already been proposed in the literature for various blood vessels (Lesage et al., 2009). In 3D vessel segmentation, most existing techniques exploit such vessel prior knowledge as tubular structures. Different image modalities, such as digital subtraction angiography, fundus photography, contrast-enhanced CT, and MRI angiography, have different characteristics of vessel features. Even in the same modality, blood vessels in different tissues may still have slight differences in feature represen-

* Corresponding author.

E-mail address: cwang@mori.m.is.nagoya-u.ac.jp (C. Wang).

tations due to signal intensity variations, inhomogeneous contrast filling, or imaging artifacts.

Conventionally, 3D local geometry features like first- and second-order derivatives of intensities are utilized. Level-set-based approaches were proposed using gradient information for blood vessel segmentation tasks (Lorigo et al., 2001; Zhu et al., 2009). Second-order derivatives information, such as the Hessian matrix, models the tubular geometric structure of blood vessels (Frangi et al., 1998; Sato et al., 1998; Kerkeni et al., 2016). The Hessian matrix is a second-order tensor; the magnitudes of its three eigenvalues indicate the local geometric structure of the image. A fair amount of approaches use Hessian-based vesselness features for tubular structure representation (Lin, 2001; Shikata et al., 2004; Wink et al., 2004; Skibbe et al., 2015). However, since Hessian tensors do not actually lie on Euclidean space. Frangi et al. and Sato et al. proposed dissimilarity measures that represent the tensor information into 1-dimensional Euclidean space (Frangi et al., 1998; Sato et al., 1998). Dimensionality reduction leads to the inaccurate modeling of geometric structure. To address this issue, many works used Hessian information associated with geometrical models (Zhu et al., 2009; Wang et al., 2010; Skibbe et al., 2015; Hanbay and Talu, 2018). Zhu et al. adopted Hessian vesselness measure as a weight parameter to construct a vascularity-oriented speed function for level-set algorithm (Zhu et al., 2009). Similarly, Hanbay et al. used Hessian eigenvalue analysis to construct a edge-stopping function for their active contour model (Hanbay and Talu, 2018). Hessian matrix has also been incorporated into the gradient vector flow model to obtain an anisotropic partial differential equation (Wang et al., 2010). Other segmentation approaches such as Markov marked-point processes (Lacoste et al., 2006; Skibbe et al., 2015) have also been used for blood vessel segmentation problems. Blood vessels are modeled as a combination of piecewise segments or particles and optimized using a Markov chain Monte Carlo algorithm (Skibbe et al., 2015) that utilizes both first- and second-order derivatives information to construct the particle. However, Markov marked-point approaches are not pixelwise, and disconnection and bifurcation problems remain to be solved. This is also a common issue for other model-fitting-based methods, including (Tyrrell et al., 2007; Friman et al., 2010; Wörz and Rohr, 2008).

The graph-cut method, which has been widely used for many such low-level computer vision problems as segmentation and registration (Boykov et al., 2001; Rother et al., 2004; Tang and Chung, 2007), can find the exact solution in polynomial time for submodular energy. However, the local neighboring Markov random field (MRF) model, where the voxels are only connected to their neighboring voxels, has a side effect, short-boundary bias, which results from the influence of the pairwise term, which penalizes the elongated boundaries. A high-order MRF model has been presented to tackle this problem by coupling similar edges (Vicente et al., 2008; Jegelka and Bilmes, 2011; Kohli et al., 2013). Many approaches have also adopted graph-cuts into blood vessel segmentation problems using additional information, such as shape prior (Bauer et al., 2010) and geometrical moments (Esneault et al., 2010).

Recently, deep-learning techniques have achieved remarkable progress in the computer vision field. Unlike the above unsupervised approaches, conventional deep-learning techniques are data-demanded, which means that many training data and annotated labels are needed. Many researches addressed 2D retinal blood vessel segmentation problems (Liskowski and Krawiec, 2016; Fu et al., 2016; Jiang et al., 2018). More recently, a 2.5D fully convolutional neural network (FCN) was successfully applied to 3D blood vessel segmentation on magnetic resonance angiography (MRA) time-of-flight (TOF) and synchrotron radiation x-ray tomographic microscopy (SRXTM) datasets (Tetteh et al., 2018).

In this study, we tackle the short-boundary bias issue by introducing tubular geometric information to the MRF model to exploit

the advantages of both graph-cut and vesselness-enhancement filtering. We propose a fully automatic blood vessel segmentation method named *tensor-cut* using a tensor-based graph-cut approach and apply it to fine renal artery segmentation. We use both intensity and tensor information to construct a first-order MRF. Using tensors for image processing can be traced back to 1980s, Bigün et al. first presented structure tensor using gradient information (Bigün, 1987; Bigün et al., 1991). Knutsson et al. presented a local energy-based method to calculate the local structure tensor by analysing the responses of a set of quadrature filters (Knutsson et al., 2011). Lindeberg et al. presented Gaussian scale-space for a multi-scale representation for tensors (Lindeberg, 1994). Our proposed method exploits the second-order information of the geometry structure of blood vessels. Unlike many existing blood vessel segmentation methods that only use the high-dimensional geometric information in low-dimensional Euclidean space, the proposed method directly utilizes the geometric information in manifold space that can contribute to a more accurate model.

This work is an extension of our previous work (Wang et al., 2016b) with a more detailed introduction to our approach and more experiments including both simulated and clinical experiments.

2. Method

2.1. Overview

This section briefly summarizes the entire algorithm whose flowchart is shown in Fig. 1. In the first stage, the input 3D volume data are filtered using a Hessian-based vesselness filter to create a tensor field. Then the Riemannian and Euclidean metrics are respectively utilized as dissimilarity measures for the tensors and the scalar intensity. In the second stage, a first-order Markov random field is constructed that consists of hidden and labeling layers. Finally, we performed a graph cuts algorithm to get the final segmentation result.

2.2. Tensor field

In one related work, Han et al. constructed a multi-scale nonlinear structure tensor (MSNST) space to extract textures from natural images (Han and Wang, 2015). First, a multi-scale structure tensor (MSST) is constructed by calculating gradient $D^s(x, y)$ (omitted as D^s) of image I at scale s :

$$\tau^s = \alpha^{-2s} \begin{bmatrix} (D_x^s)^2 & (D_x^s D_y^s) \\ (D_x^s D_y^s) & (D_y^s)^2 \end{bmatrix}, \quad (1)$$

where $s \in (0, S)$, S is the total of the scales. D_x^s and D_y^s represent two gradient components along the x and y directions. $D_x^s(x, y) = \partial(I * \theta^s)(x, y) / \partial x$, $D_y^s(x, y) = \partial(I * \theta^s)(x, y) / \partial y$. $\theta(x, y)$ is a 2D differential function, and α is a constant parameter.

Then, a nonlinear anisotropic filter (Gerig et al., 1992) is applied to each MSST to obtain the MSNST space. Each pixel in an image is represented as a MSNST T :

$$T = \{\hat{\tau}_0, \hat{\tau}_1, \dots, \hat{\tau}_{s-1}\}. \quad (2)$$

In this work, instead of using first-order structure tensor to capture the texture features, we utilize a Hessian matrix to describe the tubular geometric features. Unlike the previous work (Han and Wang, 2015), we do not construct a multi-scale tensor space. Using a multi-scale vesselness-enhancement filter, we get the best scale to represent the blood vessels. This strategy effectively reduces the computing time.

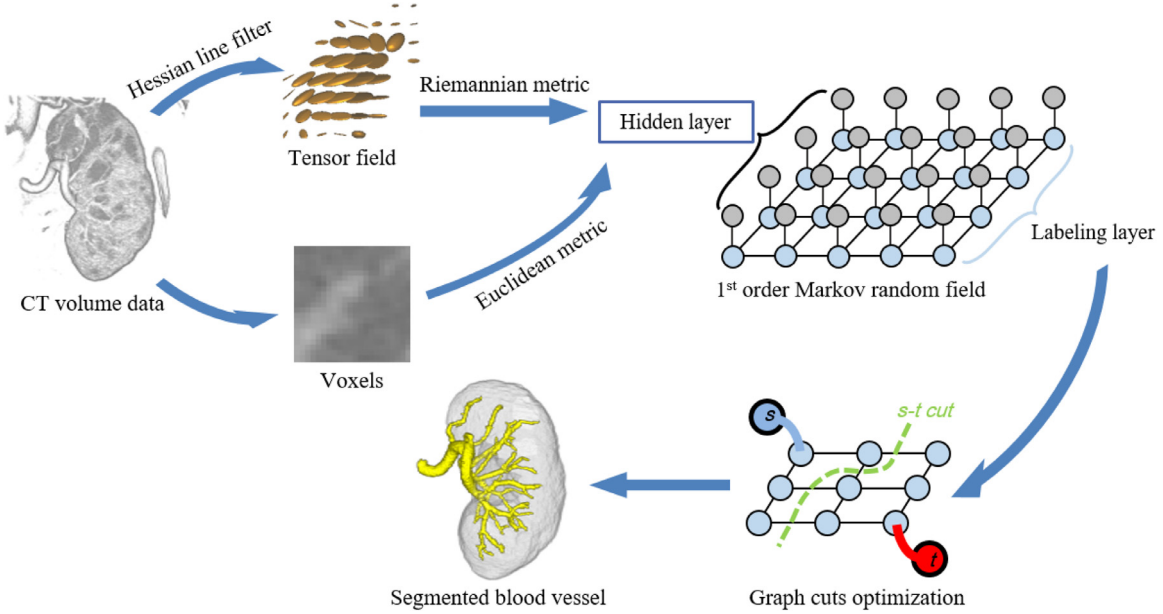


Fig. 1. Flowchart of proposed algorithm.

The 3D Hessian matrix at scale s is given:

$$\nabla^2 I^s(\mathbf{x}) = \begin{bmatrix} I_{xx}^s(\mathbf{x}) & I_{xy}^s(\mathbf{x}) & I_{xz}^s(\mathbf{x}) \\ I_{yx}^s(\mathbf{x}) & I_{yy}^s(\mathbf{x}) & I_{yz}^s(\mathbf{x}) \\ I_{zx}^s(\mathbf{x}) & I_{zy}^s(\mathbf{x}) & I_{zz}^s(\mathbf{x}) \end{bmatrix}. \quad (3)$$

Here $I^{ij}(\mathbf{x}) = \frac{\partial^2}{\partial i \partial j} I(\mathbf{x})$, ($i, j \in \{x, y, z\}$) represents the second-order partial derivatives of local image I at voxel \mathbf{x} . This symmetric matrix can resemble a second-order tensor \mathcal{T}^H . A multi-scale Hessian-based vesselness-enhancement filter (Frangi et al., 1998; Sato et al., 1998) is utilized to find the most appropriate scale to represent the tubular structure. Vesselness-measure \mathcal{V}^s at scale s is given:

$$\mathcal{V}^s = \begin{cases} |\lambda_3^s| \left(\frac{\lambda_2^s}{\lambda_3^s} \right)^{\gamma_{23}} \left(1 + \frac{\lambda_1^s}{|\lambda_2^s|} \right)^{\gamma_{12}}, & \text{if } \lambda_3^s < \lambda_2^s, \lambda_1^s \leq 0, \\ |\lambda_3^s| \left(\frac{\lambda_2^s}{\lambda_3^s} \right)^{\gamma_{23}} \left(1 - \alpha \frac{\lambda_1^s}{|\lambda_2^s|} \right)^{\gamma_{12}}, & \text{if } \lambda_3^s < \lambda_2^s, 0 < \lambda_1^s < \frac{|\lambda_2^s|}{\alpha}, \\ 0, & \text{otherwise.} \end{cases} \quad (4)$$

where λ_1^s , λ_2^s , and λ_3^s are the eigenvalues of the Hessian matrix at scale s , ($\lambda_2^s > \lambda_3^s > \lambda_1^s$). Scale $s \in (0, S)$, S is the total number of scales. γ_{12} and γ_{23} are constant parameters. α is introduced to provide an asymmetrical characteristic (Sato et al., 1998). The scale with highest vesselness-response \mathcal{V}_{\max} is the most appropriate scale to represent the blood vessels, and the most appropriate scale $s' = \operatorname{argmax}_s \mathcal{V}^s$, $s \in (0, S)$.

However, scale s' can be obtained for every voxel of image $I(\mathbf{x})$ even if its structure is not tubular. Therefore, we add a constraint to reduce these noisy tensors. In this paper, we introduce diagonal tensor \mathcal{T}^D to replace these non-vessel tensors that can be expressed:

$$\mathcal{T} = \begin{cases} \mathcal{T}^H, & \mathcal{V}_{\max} > 0 \\ \mathcal{T}^D, & \mathcal{V}_{\max} \leq 0, \end{cases} \quad (5)$$

where $\mathcal{T}^D = \begin{bmatrix} \lambda_1 & 0 & 0 \\ 0 & \lambda_2 & 0 \\ 0 & 0 & \lambda_3 \end{bmatrix}$ and $\lambda_3 \gg \lambda_2 \approx \lambda_1 > 0$. Here

\mathcal{T}^D represents a plate-like structure. This diagonal tensor provides a non-tubular tensor for those voxels that do not belong

to the tubular structures. Tensor field \mathbb{T} can be constructed. $\mathbb{T} = \{\mathcal{T}_0, \mathcal{T}_1, \dots, \mathcal{T}_n\}$, $n \in N$. $\mathcal{T}_i \in \{\mathcal{T}^H, \mathcal{T}^D\}$, $\forall i \in N$. N denotes voxel number. A visualized example of a tensor field is shown in Fig. 2 where only tubular tensors are illustrated. The tensor visualization technique was previously presented (Barmoutis et al., 2007). Ellipsoids are constructed with the eigenvalues and the eigenvectors of the Hessian matrix.

2.3. Tensor metric in Riemannian space

In this section, we briefly review Riemannian metrics for computing tensor statistics. Since second-order tensors cannot be handled by traditional linear statistical methods, non-linear metrics are required for computing statistics on tensors. In our previous work, we modeled a tensor as an ellipsoid and used Euclidean metrics to calculate the dissimilarity between ellipsoids (Wang et al., 2016a).

Many studies have studied how to perform statistics over tensor space, such as DTI images (Fletcher and Joshi, 2007; Pennec et al., 2006; Ghosh et al., 2008). Tensors are not a vector space so that traditional vector operations cannot be applied to tensor computing. Actually, the tensor space forms a type of manifold, viz., a *Riemannian manifold*. Riemannian manifolds (\mathcal{M}, g) are smooth manifolds \mathcal{M} with Riemannian metric g . A manifold consists of a series of linear Euclidean subspaces. Similar to any other curved surfaces, the geodesic distances between two vectors on a manifold is a continuous collection of projection distances in a tangent space at each point. Riemannian metric g makes it possible to calculate the statistics of the manifolds, such as mean value, geodesic distances, and geodesic interpolation.

Riemannian metrics handle symmetric positive definite (SPD) matrices, which form a convex half-cone in the vector space of the matrices. Many standard operations are stable in this space (Pennec et al., 2006). However, the Hessian matrix may have negative eigenvalues, i.e., since it is an indefinite matrix.

In our previous work (Wang et al., 2016b), we used a transformation trick to convert the indefinite Hessian matrices to SPD matrices. The transformation helps map a Hessian matrix to a Riemannian manifold. Let \mathcal{T}^- denotes an indefinite Hessian matrix with negative eigenvalues, and let \mathbf{U} denotes an invertible orthogonal matrix with columns that correspond to eigenvectors. We have

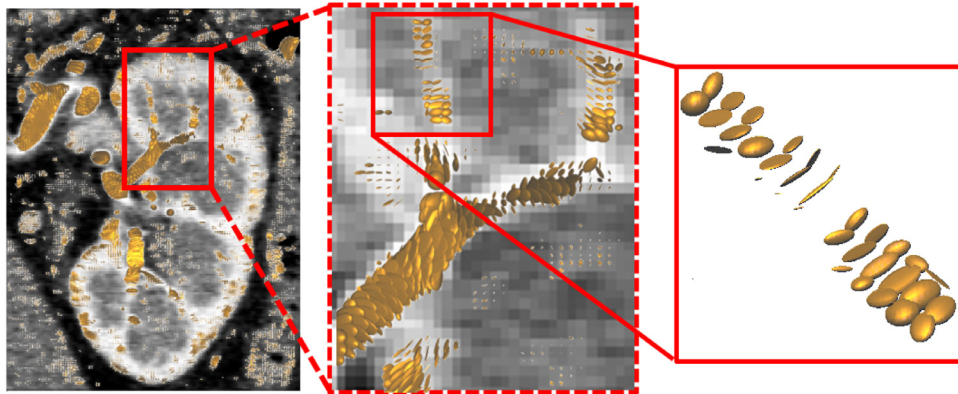


Fig. 2. Constructed tensor field of one CT slice. Only tensors with $\nu_{\max} > 0$ are shown.

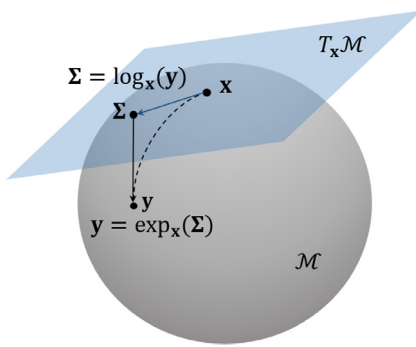


Fig. 3. Illustration of geodesic distance computing on manifold. \mathbf{x} and \mathbf{y} denote two tensors on manifold \mathcal{M} . Σ is a vector on tangent space $T_{\mathbf{x}}\mathcal{M}$ at \mathbf{x} . Σ is projected by a logarithmic mapping $\log_{\mathbf{x}}(\mathbf{y})$ from tensor \mathbf{x} to tangent space, and exponential mapping $\exp_{\mathbf{x}}(\Sigma)$ projects Σ back to manifold.

$\mathcal{T}^- = \mathbf{U}\mathbf{D}\mathbf{U}^{-1} = \mathbf{U}\mathbf{D}\mathbf{U}^T$, where \mathbf{D} is a diagonal matrix. $\mathbf{D} = \text{diag}(d_i)$, where d_i is the i -th eigenvalue. Positive definite tensor \mathcal{T}^+ can be obtained:

$$\mathcal{T}^+ = \text{abs}(\mathcal{T}^-) = \mathbf{U}\text{diag}(\text{abs}(d_i))\mathbf{U}^T, \mathcal{T}^+ \in \text{Sym}^+. \quad (6)$$

However, this transformation assumes that tensors are in ideal tubular shape: $\lambda_2 \approx \lambda_3$, $|\lambda_2| \gg |\lambda_1| \approx 0$. In this work, we directly use the absolute value of generalized eigenvalues of the tensors to transform the Hessian tensors to a semi-Riemannian space. The revised transformation is given in Eq. (7), which is more mathematically reasonable than previous transformation.

Pennec et al. (2006) and Moakher (2005) described an affine invariant Riemannian metric for statistics to compute SPD matrices (tensors). As shown in Fig. 3, the geodesic path between tensors \mathbf{x} and \mathbf{y} on manifold \mathcal{M} is the shortest curve shown in the dotted line. The geodesic distance is defined as $d(\mathbf{x}, \mathbf{y}) = \|\bar{\mathbf{x}}\bar{\mathbf{y}}\|_{\mathbf{x}}$. $\bar{\mathbf{x}}\bar{\mathbf{y}}$ is a vector in tangent space $T_{\mathbf{x}}\mathcal{M}$, which is projected by a logarithmic mapping: $\bar{\mathbf{x}}\bar{\mathbf{y}} = \log_{\mathbf{x}}(\mathbf{y})$. In our case, the geodesic distance between two tensors can be written:

$$d(\mathcal{T}_1, \mathcal{T}_2) = \|\log_{\mathcal{T}_1}(\mathcal{T}_2)\|_{\mathcal{T}_1} = \left(\sum_{i=1}^d \log^2 \text{abs}(\lambda_i(\mathcal{T}_1, \mathcal{T}_2)) \right)^{\frac{1}{2}}, \quad (7)$$

where $\lambda_i(\mathcal{T}_1, \mathcal{T}_2)$ is the generalized eigenvalues of tensors \mathcal{T}_1 and \mathcal{T}_2 . d denotes the order of the SPD matrix, which is $d = 3$. Actually, Eq. (7) is a kind of semi-Riemannian metric (a.k.a pseudo-Riemannian metric) to handle our Hessian matrices. Semi-Riemannian manifold, is a differentiable manifold, in which the requirement of SPD constraint is relaxed. In semi-Riemannian space, tensors need not be positive definite at every point which allows us to calculate semi-distance between Hessian tensors.

We calculated the mean and the variance of the tensors using the same method given in a previous work (Pennec et al., 2006). A simple introduction is described in the appendix. A more detailed description is also available (Pennec et al., 2006).

2.4. Graph-cut using tensors

A graph-cut is a powerful optimization tool for solving low-level vision problems (Boykov et al., 2001; Boykov and Jolly, 2001). Based on the max-flow/min-cut theorem, the minimum cut that corresponds to the best solution of a sub-modular energy function can be found in polynomial time. A traditional graph-cut is based on a first-order Markov random field (MRF), which means that only adjacent nodes are considered. This graphical model easily leads to a short-boundary bias. For blood vessel segmentation problems, this short-boundary bias causes serious under-segmentation of tiny blood vessels. This problem can be addressed with a high-order MRF instead of a first-order MRF considering high-order cliques can also effectively avoid local minimum cuts (Kohli et al., 2013; Jegelka and Bilmes, 2011). Another direct method to avoid short-boundary bias is to make a more accurate objective distribution model to prevent local minimal cuts. In this paper, we use the local geometric information presented as tensors to improve the accuracy of the GMM model.

The minimum cut problem, also known as $s - t$ cut, needs pre-specified source nodes (s nodes) and sink nodes (t nodes). However, for 3D blood vessel segmentation, manually creating these terminal nodes is time-consuming (including s and t nodes). In this work, we automatically generate terminal nodes using K-means algorithm. Let $I_V(\mathbf{x})$ be an image filtered by a vesselness-enhancement filter, and then we extract the most probable blood vessel region as s nodes with K-means clustering. The most probable cluster \mathbf{c}'_{\max} is given:

$$\mathbf{C}' = \underset{\mathbf{C}}{\operatorname{argmin}} \sum_{i=1}^K \sum_{\mathbf{x} \in \mathbf{c}_i} \|I_V(\mathbf{x}) - \bar{I}_{\mathbf{c}_i}\|^2, \mathbf{c}_i \in \mathbf{C} \quad (8)$$

$$\mathbf{c}'_{\max} = \underset{\mathbf{c}'_i}{\operatorname{argmax}} \frac{1}{|\mathbf{c}'_i|} \sum_{\mathbf{x} \in \mathbf{c}'_i} |I_V(\mathbf{x})|, \mathbf{c}'_i \in \mathbf{C}', \quad (9)$$

where \mathbf{c}_i is the i -th cluster of total K clusters \mathbf{C} . $\bar{I}_{\mathbf{c}_i}$ denotes the mean intensity of the voxels in cluster \mathbf{c}_i . \mathbf{C}' is the final clusters. In Eq. (9), cluster \mathbf{c}'_{\max} with the highest mean intensity is selected as the foreground region: the s nodes. In practice, cluster number K is set to five in this paper. An example of a generated foreground region is shown in Fig. 4. For the possible background region, we first dilate the foreground region with radius $r = 3$ and use the complement of the dilated foreground region as a possible background region (t nodes).

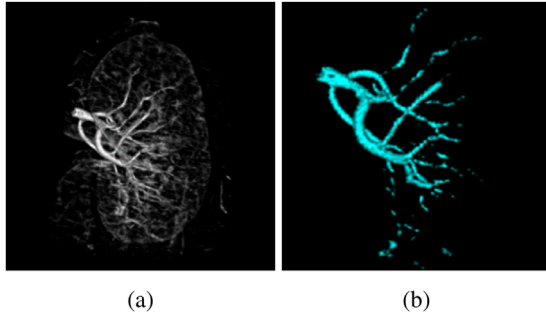


Fig. 4. Generated foreground region using K-means clustering: (a) Vesselness-enhancement result $I_v(\mathbf{x})$. (b) Most probable blood vessel region \mathbf{c}'_{\max} extracted using K-means ($K = 5$).

Same as previous work (Rother et al., 2004), for improved accuracy, we used a Gaussian mixture model (GMM) to estimate the probability distribution of the blood vessels and the background region instead of histogram approaches. Two GMMs with K_g components are required: one for the foreground region and another for the background region. A GMM can generally be written as $\Pr(u) = \sum_k \eta_k \mathcal{N}(u|\mu_k, \sigma_k)$ ($k \in K_g$). $\mathcal{N}(u)$ denotes the Gaussian distribution. η_k is a weight parameter for each Gaussian component. GMMs for intensity and tensors are given:

$$\begin{aligned} \Pr(\mathbf{x}) &= \sum_{k=1}^{K_g} \gamma_k \mathcal{N}(\mathbf{x}|\bar{I}^k, \sigma_I^k) \\ \Pr(\mathcal{T}) &= \sum_{k=1}^{K_g} \theta_k \mathcal{N}(\mathcal{T}|\bar{\mathcal{T}}^k, \sigma_T^k) \end{aligned} \quad (10)$$

where \bar{I} and σ_I denote the mean and the variance of the intensity. $\bar{\mathcal{T}}$ and σ_T denote the mean and the variance of the tensors; detailed descriptions are given in the appendix. γ and θ are weight parameters that can be obtained using the EM algorithm (Dempster et al., 1977).

For a graph-cut, we utilized both the intensity and tensor information. The energy function is described:

$$\begin{aligned} E(L) = & \underbrace{\sum_{\mathbf{x} \in \mathbb{X}} -\log \Pr(L_x|\mathbf{x})}_{\text{data term}} + \lambda_I \underbrace{\sum_{\{\mathbf{x}_m, \mathbf{x}_n\} \in \mathcal{N}} V_{m,n}(\mathbf{x}_m, \mathbf{x}_n)}_{\text{smoothness term}} \\ & + \underbrace{\omega \left(\sum_{\mathcal{T} \in \mathbb{T}} -\log \Pr(L_{\mathcal{T}}|\mathcal{T}) + \lambda_T \sum_{\{\mathcal{T}_m, \mathcal{T}_n\} \in \mathcal{N}'} U_{m,n}(\mathcal{T}_m, \mathcal{T}_n) \right)}_{\text{tensor term}} \end{aligned} \quad (11)$$

where $L = \{L_F, L_B\}$ denotes labels and L_F and L_B are foreground and background labels. ω represents the weight parameter to adjust the weight between the intensity and tensor term energy. The λ_I and λ_T parameters adjust the weight between the data term and the smoothness term in the graphical model. $\Pr(L_x|\mathbf{x})$ and $\Pr(L_{\mathcal{T}}|\mathcal{T})$ denote conditional probabilities of voxels \mathbf{x} and tensors \mathcal{T} derived using Bayes rule. In this paper, we use a first-order MRf, which means that we only consider the edges between neighboring voxels. \mathcal{N} and \mathcal{N}' denote pair sets of neighboring voxels and tensors. $V_{m,n}(\cdot, \cdot)$ and $U_{m,n}(\cdot, \cdot)$ denote a dissimilarity measure for a pair of neighboring voxels and tensors: the energy of the edges. The dissimilarity measure for both voxels and tensors are given:

$$\begin{aligned} V_{m,n}(\mathbf{x}_m, \mathbf{x}_n) &= \frac{\exp(-\xi d^2(\mathbf{x}_m, \mathbf{x}_n))}{\text{dist}(\mathbf{x}_m, \mathbf{x}_n)} \\ U_{m,n}(\mathcal{T}_m, \mathcal{T}_n) &= \frac{\exp(-\xi d^2(\mathcal{T}_m, \mathcal{T}_n))}{\text{dist}(\mathcal{T}_m, \mathcal{T}_n)} \end{aligned} \quad (12)$$

where ξ is a constant parameter that can be estimated as the noise level and $\text{dist}(\cdot, \cdot)$ denotes the Euclidean distance between two voxels or tensors, i.e. the physical distance between two points.

Finally, the minimum cut can be found by the graph-cut algorithm for a given energy function in Eq. (11). The terminal nodes belonging to the source are the final segmentation result. A simple pseudocode for our tensor-based graph-cut is shown in Algorithm 1.

Algorithm 1 Tensor-based graph-cut.

```

Input:  $\mathbf{x} \in I, \mathcal{T} \in \mathbb{T}$ 
Output: Segmentation  $L = \{L_F, L_B\}$ 
Initialize:  $\tilde{\mathcal{T}}_0 = \mathcal{T}_1, t = 0, \epsilon = 0.001$ 
Calculate
   $\mathbf{c}'_{\max}$  ▷ Terminal nodes (Eq. 9)
   $\Pr(\mathbf{x}), \Pr(\mathcal{T}), (\mathbf{x} \in \mathbf{c}'_{\max}, \mathcal{T} \in \mathbf{c}'_{\max})$  ▷ GMM (Eq. 10)
   $-\log \Pr(L_x|\mathbf{x}), -\log \Pr(L_{\mathcal{T}}|\mathcal{T})$  ▷ Data terms
   $V_{m,n}(\mathbf{x}_m, \mathbf{x}_n), U_{m,n}(\mathcal{T}_m, \mathcal{T}_n)$  ▷ Smoothness terms
   $L \leftarrow \text{min-cut/max-flow algorithms (Boykov and Jolly, 2001)}$ 

```

3. Experiments

3.1. Material

In this paper, we did experiments both on simulated data and on clinical contrast-enhanced CT data to validate our proposed algorithm.

We used eleven cases of phantom data, all of which were generated using a public tubular structure generator called vascular synthesizer (*VascuSynth*) (Hamarneh and Jassi, 2010), which is a simulated vascular synthesizer that generates vascular structure based on such user-defined vascular properties as bifurcation number, oxygen demand map, and other tunable parameters. To the best of our knowledge, *VascuSynth* is the state-of-the-art vascular synthesizer in the literature. However, public vascular datasets¹ have few bifurcation nodes, which can easily be segmented by all methods. Therefore, we generated the phantom datasets with more bifurcation nodes and small bifurcation angles. Four generated pieces of phantom data are shown in Fig. 5. In this work, we generated phantom data with different bifurcation numbers that ranged from 200 to 400, and oxygen demand maps and other parameters were randomly decided. Gaussian white noise was added to obtain the final simulated data. We added two noise levels to each phantom data with Gaussian variations $\sigma_n = 0.3$ and 0.8 ; Thus in the simulated experiments, we have 22 synthetic datasets. To make the simulated data more closely resemble the clinical CT data, we applied a Gaussian-smoothing filter with a 2.0-mm radius to the phantom data. An example of the final generated data is shown in Fig. 6. Compared to its original phantom data without noise, many tiny vascular structures are lost by applying with noise and smoothing filters. The sizes of all the 22 simulated bits of data are $160 \times 160 \times 160$ with identical resolution $1.0 \times 1.0 \times 1.0$ mm³.

We used 19 cases of clinical CT data for the experiments and focused on the renal artery segmentation problem. As pre-processing for the clinical CT data, the volumes of interest (VOIs) of the kidney region were extracted manually. One bit of VOI data contains an entire kidney region. One example of kidney VOI data is shown in Fig. 7. Detailed VOI data specification is summarized in Table 1.

¹ <http://vascusynth.cs.sfu.ca>

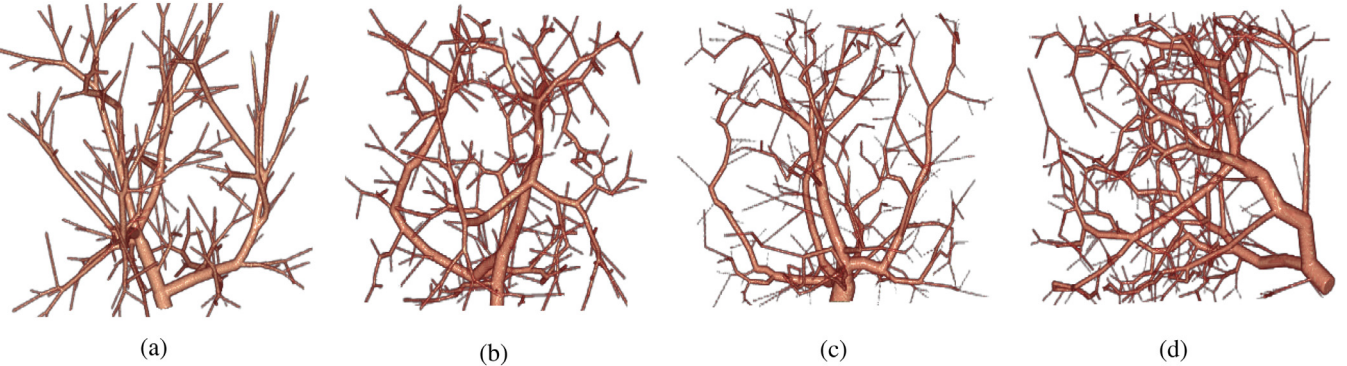


Fig. 5. Four phantom vascular pieces of data generated by *VascuSynth* with different bifurcation numbers: (a), (b), (c), and (d) respectively have 200, 250, 300, and 400 bifurcations.

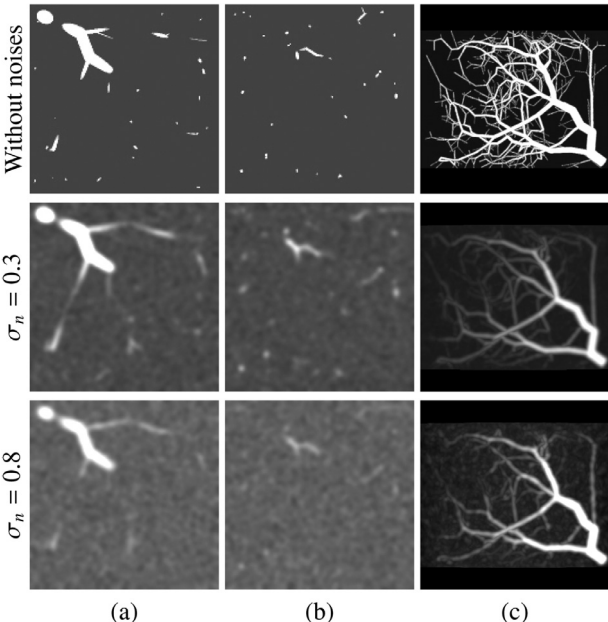


Fig. 6. Examples of final simulated data: Original phantom data without noise are shown in first row. Simulated data in second row are applied with white noise of $\sigma_n = 0.3$, and third row is applied with $\sigma_n = 0.8$. (a) and (b) two axial slices of the simulated data. (c) maximum intensity projection (MIP) images. Compared to original phantom data, many details are lost by adding white noise and smoothing.

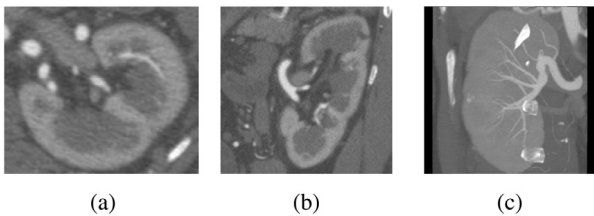


Fig. 7. Volume of interest showing kidney in CT data: (a) and (b) one axial and sagittal slice, respectively. (c) MIP of image of VOI data.

Table 1
Kidney VOI specification.

Slice size [pixels]	$(98 - 166) \times (90 - 148)$
Slice number [slices]	157 - 270
Pixel spacing [mm]	0.5 - 0.7
Slice pitch [mm]	0.4 - 0.8

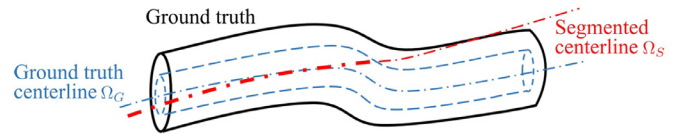


Fig. 8. Illustration of calculation of centerline overlap CO. Tubular structure in black is gold standard blood vessel, and its centerline $\Omega_G(\mathbf{x})$ is shown as blue \dash-dot line. Tube $\mathcal{U}(\mathbf{x})$ is generated by dilating centerline of a two-voxel radius. Red dash line denotes centerline of segmented vessels $\Omega_S(\mathbf{x})$.

3.2. Measurements

We used three types of measurements to validate the segmentation performances in this work: sensitivity (Se), specificity (Spc), centerline overlap (CO), and centerline error (CE). Se , or the true positive rate (TPR), measures the algorithm's ability to correctly extract the target region (blood vessels). Spc , or the true negative rate (TNR), refers to its ability to correctly extract the background region (non-blood vessels). Se and Spc are given:

$$Se = \frac{TP}{TP + FN}, \quad Spc = \frac{TN}{TN + FP}, \quad (13)$$

where TP , FN , TN , and FP respectively denote the voxel numbers of true positives, false negatives, true negatives, and false positives.

The Dice coefficient (DC) (Dice, 1945) is generally used for evaluating the overlap between the ground truth and segmentation results. However, the DC metric is heavily influenced by the volume of the target region (Rohlfing, 2012). A small volumetric variation of segmented, thick blood vessels may have greater influence than the volumetric variation of tiny blood vessels. Therefore, instead of DC, we introduce the CO index to improve the accuracy evaluation for tiny blood vessel segmentation and use centerline overlap measures (Metz et al., 2008). Fig. 8 describes how to calculate the centerline overlap ratio. $\Omega_G(\mathbf{x})$ and $\Omega_S(\mathbf{x})$ denote the centerlines of the ground truth and segmentation results, respectively. Overlap region $O_\Omega = \{\mathbf{x} | \mathbf{x} \in \Omega_S(\mathbf{x}) \cap \mathbf{x} \in \mathcal{U}(\mathbf{x})\}$, where $\mathcal{U}(\mathbf{x})$ is dilated $\Omega_G(\mathbf{x})$ with a two-voxels radius. The CO index is given:

$$CO = \frac{2 * \|O_\Omega\|}{\|\Omega_G\| + \|\Omega_S\|}, \quad (14)$$

where $\| \cdot \|$ represents the length.

Centerline error (CE) has also been used in many blood vessel segmentation works (Metz et al., 2008; Moccia et al., 2018) especially for coronary artery which needs quantitative analysis. CE mainly measures the distance between segmentation and ground truth. In this work, our CE index is defined:

$$CE = \frac{h(\Omega_G(\mathbf{x}), \Omega_S(\mathbf{x})) + h(\Omega_S(\mathbf{x}), \Omega_G(\mathbf{x}))}{2}, \quad (15)$$

where $h(\cdot)$ denotes average centerline distance, e.g., $h(\Omega_G(\mathbf{x}), \Omega_S(\mathbf{x})) = \frac{1}{\|\Omega_G\|} \sum_{p_G \in \Omega_G} \min_{p_S \in \Omega_S} (|p_G - p_S|)$. For both CO and CE, we only compute the scores on the longest connected vascular trees. Pre-processing is performed to extract the maximum connected voxels. Tensor-cut has three primary parameters that must be specified: λ_I , λ_T , and ω . In both simulated and clinical experiments, we performed a grid search to select these three parameters and to plot the upper bounds of all the results in the ROC curves.

3.3. Reference approaches

We consider six reference approaches in this paper. As the basic ideas of our proposed method, evaluations of the classic vesselness-enhancement filter (VEF) (Sato et al., 1998) and the graph-cut algorithm (GC) (Boykov and Jolly, 2001) are critical for proving the effectiveness of our proposed method. Our method is benchmarked against four competing state-of-the-art unsupervised blood vessel segmentation methods: multiscale spherical flux (MSF) (Law and Chung, 2009), multiple hypothesis tracking (MHT) (Friman et al., 2010), super-ellipsoids (SE) (Tyrrell et al., 2007), and commercial image processing software AMIRA3-D (2019).

VEF: VEF's two main parameters, α_V and γ_V , control the trade-off between branch detection and noise suppression. Based on a previous work (Sato et al., 1998), $\alpha_V = 0.25$ and $\gamma_V = 1.0$ can optimize the trade-off and get robust results. We used this parameter setting for all the experiments in this paper, including both the simulated and clinical CT data. Since VEF is an enhancement filter, we manually threshold the segmentation results to get the best binary segmentation result for a quantitative evaluation. We implemented VEF in C++ based on a previous work (Sato et al., 1998).

GC: Unlike an interactive segmentation scheme (Boykov and Jolly, 2001), we still use the automatic segmentation scheme cited in Section 2.4. The foreground seed region is calculated by K-means, and the possible background region is the complement region of the dilated foreground region. GMM estimates the posterior probability. The energy function is identical as Eq. (11) without tensor terms. GC was implemented mainly based on a previous work (Boykov and Jolly, 2001).

MSF: Law et al. presented an efficient implement of a multiscale spherical flux computation method (Law and Chung, 2009), which is useful for practical vascular segmentation problems. Multiscale spherical-flux based method was first proposed by Vasilevskiy and Siddiqi (2002). By measuring the gradient flux through the boundaries of multiscale spheres, divergence of image gradients can be calculated. The maximum response can be obtained when the sphere is located at the centerline of blood vessel with radius same with blood vessel. To accelerate the computation speed, a multiscale spherical flux computation is performed in the Fourier domain. Vesselness is directly formulated to the response of the spherical flux. Similar to other methods (Frangi et al., 1998; Sato et al., 1998), MSF is a vascular enhancement filter. An appropriate threshold is needed to obtain the final binary segmentation result. 0.005 is the best threshold value for clinical experiments on MRA data (Law and Chung, 2009). We used the public Matlab implementation provided by Law et al.²

SE: SE is a typical model-fitting-based tubular structure segmentation method. A combination of parameterized superellipsoid and intensity appearance model is built for representing tubular structures. Maximum-likelihood method is used to estimate the parameters of superellipsoid models. The corresponding between vessel model and real blood vessel is verified using a generalized likelihood ratio test. Tracking starts from the multiple random seed

points for experiments on clinical data and only evaluates the segmentation results inside the kidney mask are evaluated. Model fitting is performed using cylindrical super-ellipsoids to detect the tubular structures. The algorithm was implemented on their Farsight software platform³. We used the default parameters in our experiments except for the detection radii.

MHT: MHT obtained the highest score in the coronary artery centerline extraction challenge (Schaap et al., 2009). Unlike the SE method, a template vessel model is designed based on Gaussian line appearance model instead of super-ellipsoids. Student *t*-test is used to verify the corresponding instead of likelihood ratio test used in SE. To avoid early stopping caused by a local minimum score, MHT introduces a multiple hypothesis tracking scheme to further improve the segmentation accuracy. The multiple hypothesis approach starts multiple tracking process in parallel, and keep the tracking with the maximum score as the success tracking. The implementation we used is provided on their MeVisLab software platform⁴. The pruning and termination thresholds are the two primary parameters that affect the segmentation performance. In our experiments, the termination thresholds were set twice as high as the pruning thresholds, based on the official suggestion (Friman et al., 2010). Since MHT is a semi-automatic method, the initial seed points must be manually specified. For all the experiments, we randomly put ten seed points at each branch level.

AMIRA: AMIRA is commercial biomedical software for visualization and image processing (AMIRA3-D, 2019). We used a module named AutoSkeleton for segmentation and implemented a vascular structure segmentation method (Fouard et al., 2006) that can extract the skeleton and the diameter of tubular structures with a distance map. First, distance map is computed using adjusted chamfer distance (Fouard and Malandain, 2005). Then, centerline and diameter are calculated using adapt distance ordered homotopic thinning (DOHT) algorithm. In this, work, we directly applied thresholding to distance maps to obtain the final binary segmentation results.

3.4. Experimental results on simulated data

We tested the segmentation methods on 22 simulated pieces of data, including two noise levels for each phantom data. The objective of the simulated experiments is to evaluate the general segmentation ability of the tubular structures. Experiments with different noise levels can evaluate the robustness against the noise. The receiver operating characteristic (ROC) curve of three cases is shown in Fig. 9. The x- and y-axes denote 1 - Spc (FPR) and Se (TPR), both of which are measured voxel-wise. No post-processing is performed on the segmentation results. As for methods which have multiple parameters, such as TC and SE, the ROC curves indicate the upper bound of all experimental results using grid-search approach. From the ROC curves, tensor-cut (TC) and MSF have the best performances among the six tested methods on the simulated dataset with a noise level of $\sigma_n = 0.3$. However, TC outperformed MSF on the simulated data with a noise level of $\sigma_n = 0.8$, which proved its robustness against different noise levels.

Experimental results showed that TC had better performances than GC and VEF, which proves the effectiveness of our proposed method. ROC indicates that the TC curves extended the GC curves, which means that TC extracted more structures than GC; i.e., introducing a tensor term effectively suppresses the short-boundary problem.

The best results (top-left of the ROC curve) of the two cases are visualized in Fig. 10. From the visualized results, TC outper-

² <http://www.cse.ust.hk/~maxlawwk/>

³ <http://www.farsight-toolkit.org/>

⁴ <https://www.mevislabs.de>

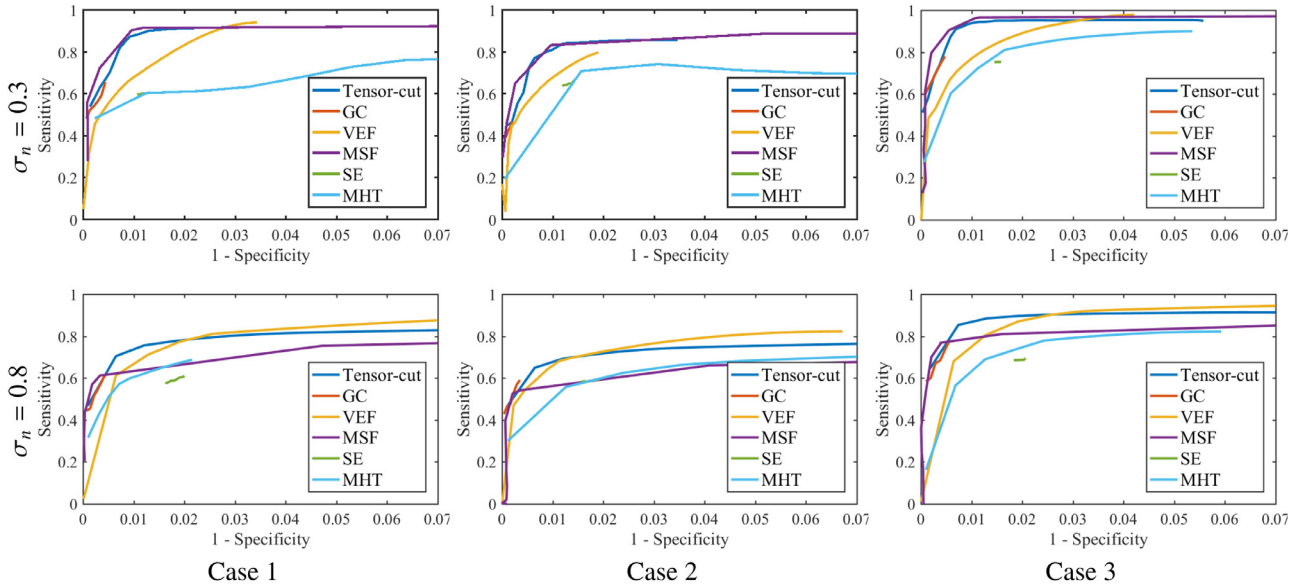


Fig. 9. ROC curves of three simulated vascular data generated by *VasculSynth* with different bifurcation number. Cases 1, 2, and 3 have 250, 300, and 350 bifurcations. Experimental results of two noise levels ($\sigma_n = 0.3$ and $\sigma_n = 0.8$) are shown in first and second rows.

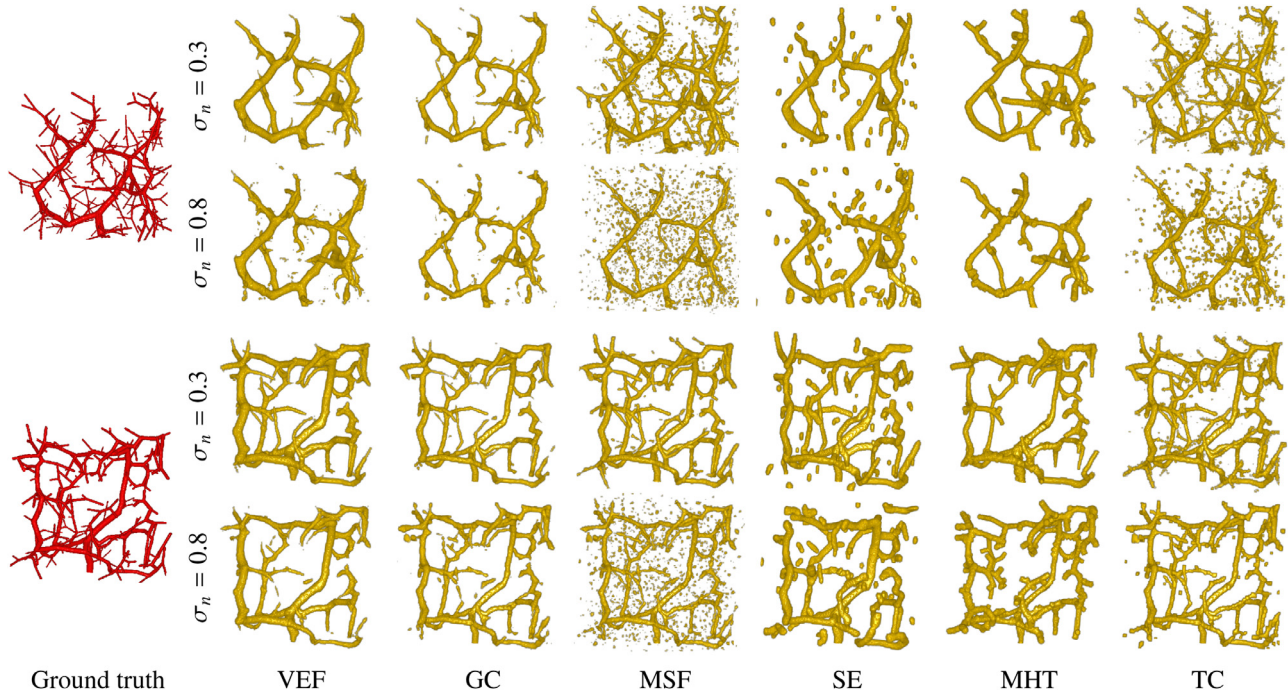


Fig. 10. Segmentation results of simulated data of Cases 1 and 3. For each, segmentation results of two noise levels ($\sigma_n = 0.3$ and $\sigma_n = 0.8$) are shown in the first and second rows.

manced the other approaches. VEF and GC under-segmented the tiny tubular structures. MSF also has good sensitivity, although it is susceptible to noise. MSF achieved similar segmentation results to TC under the $\sigma_n = 0.3$, but underperformed TC under $\sigma_n = 0.8$ condition. The model-fitting-based methods (SE and MHT) are limited to the detection of small tubular structures. ROC also showed that SE and MHT obtained poor results under both two noise levels. The quantitative statistical results of all 22 simulated bits of data are given in Table 2 that show the mean Se and Spc with their respective standard deviations.

Table 2

Quantitative statistical results of simulated dataset. Two noise levels with $\sigma_n = 0.3$ and $\sigma_n = 0.8$ are shown in two columns for each approach. Mean sensitivity, specificity, and centerline errors with their standard deviations are also shown.

	Se (%)	Spc (%)	CE (mm)
	$\sigma_n = 0.3$	$\sigma_n = 0.8$	$\sigma_n = 0.3$
TC	85.5 ± 3.8	75.3 ± 5.4	99.2 ± 0.1
GC	62.2 ± 7.6	66.0 ± 6.4	99.8 ± 0.1
VEF	72.9 ± 4.2	71.2 ± 4.2	98.9 ± 0.2
MSF	87.2 ± 4.2	64.5 ± 6.2	99.0 ± 0.2
SE	67.0 ± 5.1	64.2 ± 5.3	98.7 ± 0.1
MHT	68.0 ± 7.2	60.7 ± 5.6	98.8 ± 0.2
			$\sigma_n = 0.8$
TC	99.3 ± 0.1	1.65 ± 0.23	2.82 ± 0.91
GC	99.6 ± 0.2	5.57 ± 1.98	5.16 ± 1.67
VEF	99.0 ± 0.1	1.57 ± 0.57	3.07 ± 1.09
MSF	99.6 ± 0.1	1.96 ± 0.50	3.84 ± 1.13
SE	98.3 ± 0.1	8.81 ± 3.46	8.09 ± 1.78
MHT	98.8 ± 0.2	3.54 ± 1.22	5.40 ± 1.22

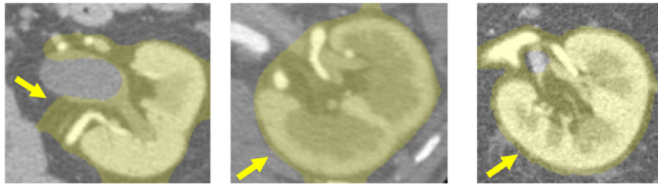


Fig. 11. Three kidney VOIs with masks, which overlap in yellow. (For interpretation of the references to colour in this figure legend, the reader is referred to the web version of this article.)

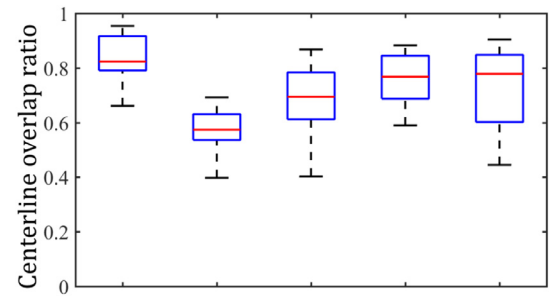
3.5. Experimental results on clinical CT data

We performed experiments on the 19 clinical CT data (VOI data). To increase the algorithm's focus on the renal arteries, we manually created a kidney mask using the standard graph-cut algorithm (Boykov and Jolly, 2001). Several cases with kidney mask overlapping are shown in Fig. 11. In this work, we also included the outside, thick renal arteries to mask.

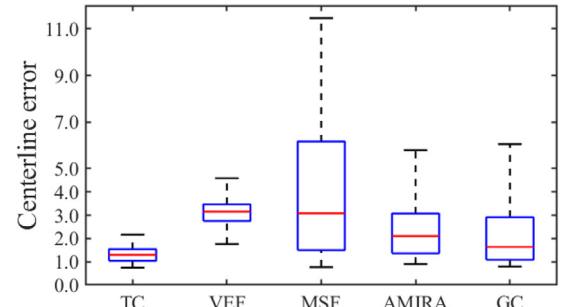
In clinical experiments, the SE and MHT methods did not achieve comparable results on the clinical dataset. The latter only extracted one or two main thick branches, and the former failed to extract renal arteries. Therefore, we omitted these two methods from our comparisons in the clinical experiments. We give the CO curves (CO against False Positive) in Fig. 12. Although the performances on the simulated and clinical data are different, our proposed method (TC) almost got the best segmentation performances. The quantitative CO and CE evaluation of 19 cases is demonstrated in Fig. 13. The TC method outperformed the other methods, and its performances are more robust. Several volume rendering results are given in Fig. 14. For each case, we show the segmentation results with the highest CO indices. Our method obtains a stable high performance, especially for tiny blood vessels.

4. Discussions

Our experiment results on both the simulated and clinical CT data show a high performance of the tensor-cut method for tubular structure segmentation. In this study, we used both the ROC curves



(a) CO



(b) CE

Fig. 13. Quantitative evaluation of 19 clinical cases. For each case, we selected the best segmentation results with the highest CO index and the lowest CE index. Red lines indicate median values, and tops and bottoms of blue boxes indicate 25th and 75th percentiles. Upper and lower bounds indicate maximum and minimal CO and CE values. (For interpretation of the references to colour in this figure legend, the reader is referred to the web version of this article.)

(TPR against FPR) and the CO curves (CO against FP) to evaluate the performances of the methods. The ROC curves measure the general segmentation ability, and the CO curves measure the segmentation ability for tiny tubular structures.

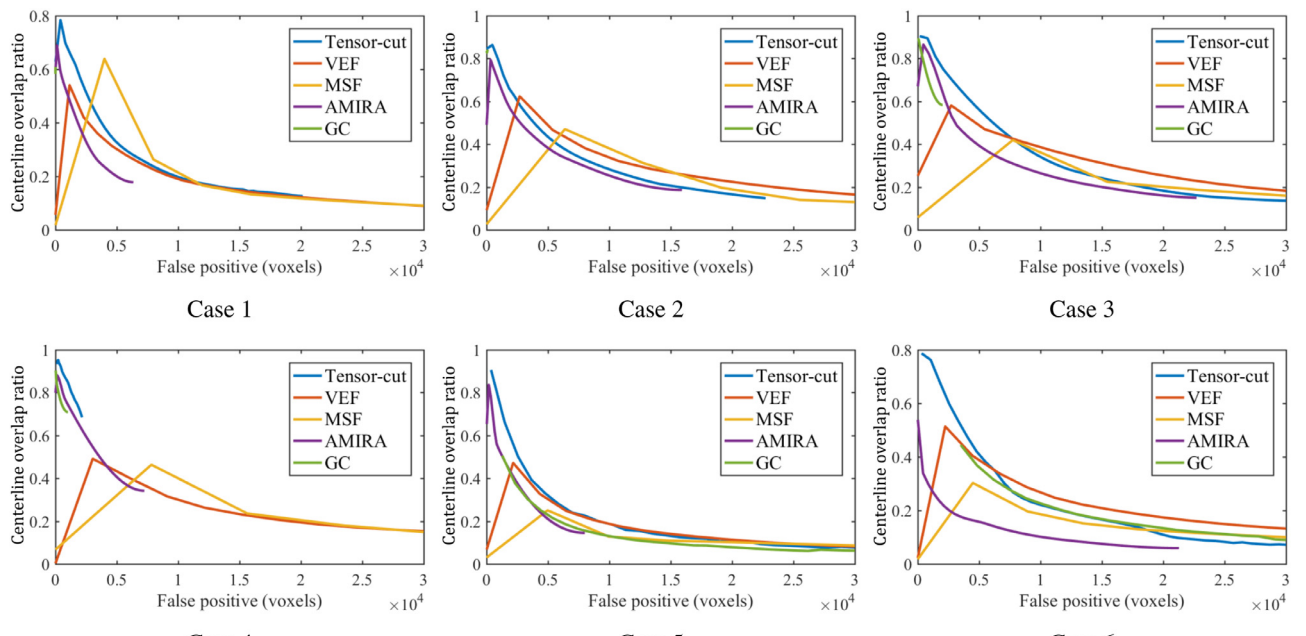


Fig. 12. CO curves of six clinical cases whose respective volume rendering results are shown in Fig. 14.

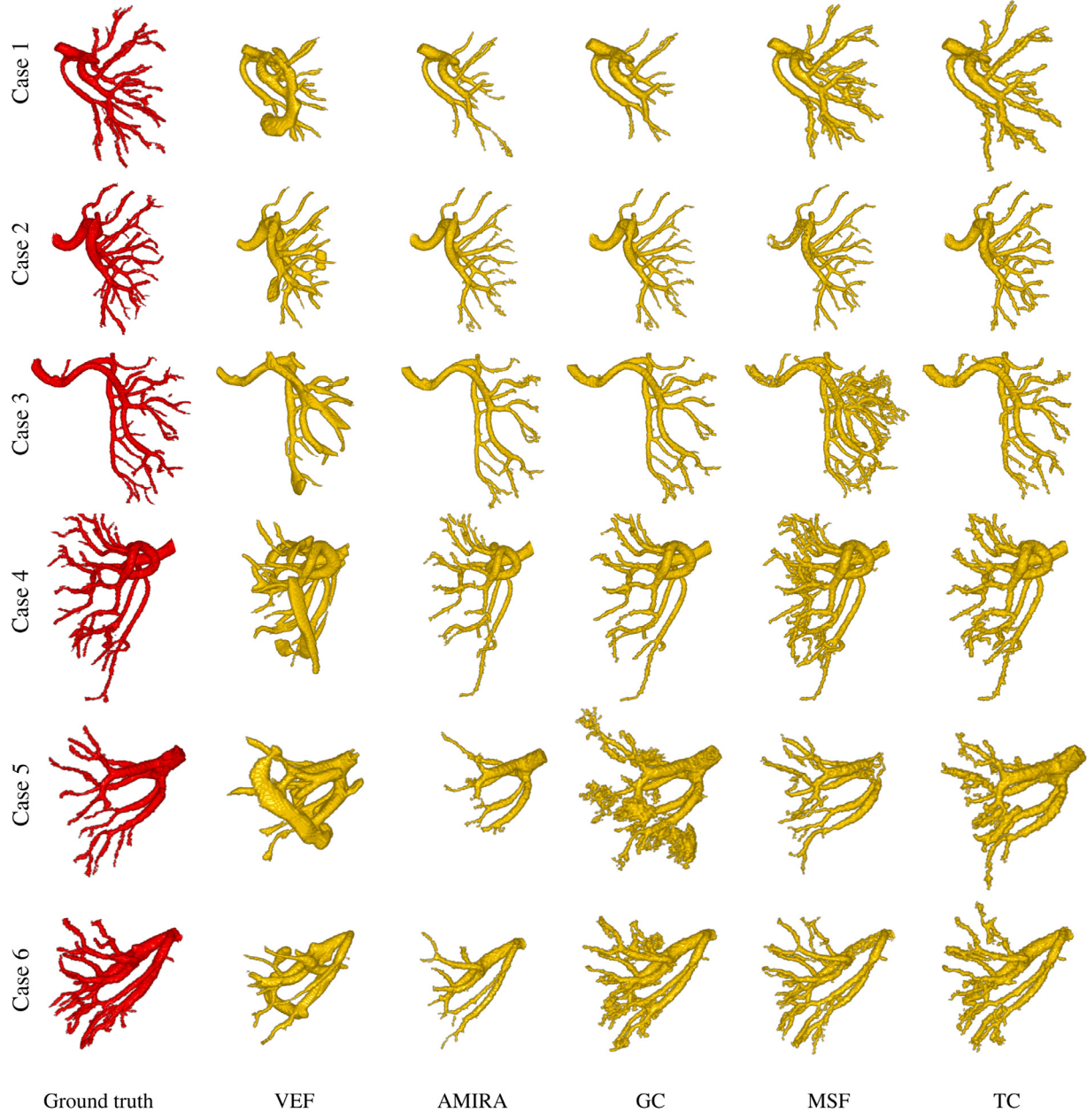


Fig. 14. Volume rendering of six clinical cases corresponding to the same cases in Fig. 12.

Our experiments on simulated data show the segmentation ability for general tubular structures. In Table 2, the experimental results with a noise level of $\sigma_n = 0.3$ show that TC and MSF outperformed all the reference approaches. However, on the noisier simulated data with a noise level of $\sigma_n = 0.8$, TC and VEF outperformed the other reference approaches. The experimental results with different noise levels indicate that TC is robust to noise and has a stable, higher performance than the other reference approaches. From Fig. 10, we identified the limitations of the ability of the model-fitting-based methods (SE and MHT) to segment tiny structures. This weakness results from the size limitation of a single vascular model. Other voxel-wise methods (including TC) do not suffer from this weakness.

Our experiments on clinical CT data aim to show the segmentation ability of blood vessels in actual clinical scenes. We show several detailed CO curve comparisons of all the reference approaches (Fig. 12) and the overall quantitative CO and CE evaluation of 19

clinical cases (Fig. 13). Fig. 12 shows the robustness of TC against the parameter variations. In Fig. 13, we plot the best CO and CE index of each case. TC achieved the best and most robust segmentation performance of all the reference approaches. TC's mean CO index is 84.0% and outperformed the second best GC of 73.2%. TC's mean CE is 1.37mm outperforming the second best GC of 2.11mm.

We show several detailed segmentation results on actual clinical CT slices in Fig. 15. The arrows indicate tiny renal arteries with small radii and low contrast against the surrounding renal cortex. Although these tiny renal arteries are easily overlooked by humans, our proposed method can segment them.

Similar to the simulated experimental results, TC outperformed the GC and VEF methods in the clinical experiments. GC achieved good segmentation results in Cases 2, 3, and 4 because high-quality CT angiographic data simplify the generation of good initial terminal nodes that contain tiny tubular structures. We show detailed comparison results of Cases 1 and 3 in Fig. 16 to evaluate

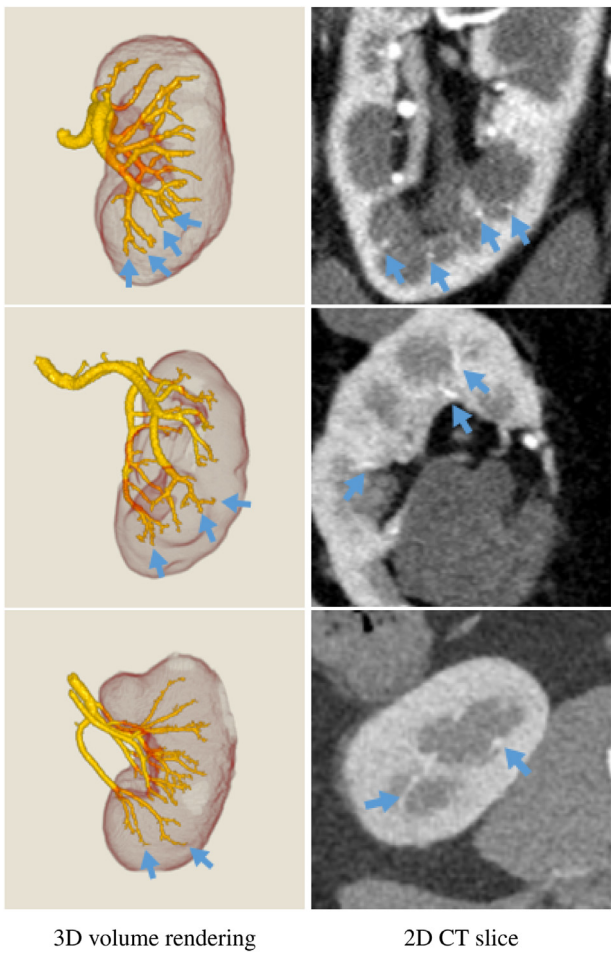


Fig. 15. Segmentation performances on CT slices: Segmented tiny blood vessels are indicated by arrows on CT slices. These tiny renal arteries can be extracted by our proposed method.

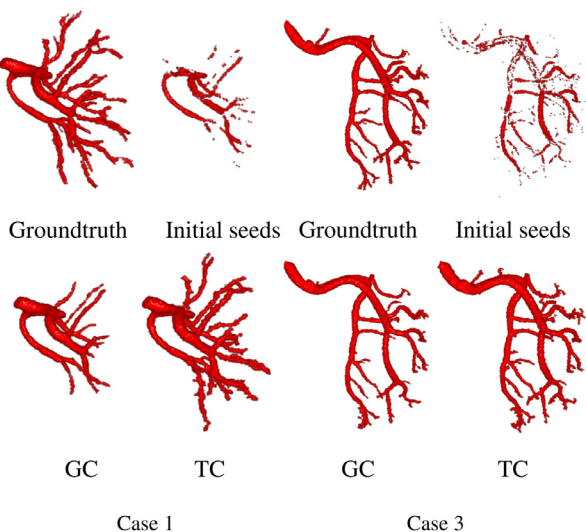


Fig. 16. Comparison between GC and TC on clinical Cases 1 and 3: Initial foreground seed voxels (s nodes) are shown in upper-right. Segmentation results of GC and TC are shown in lower rows.

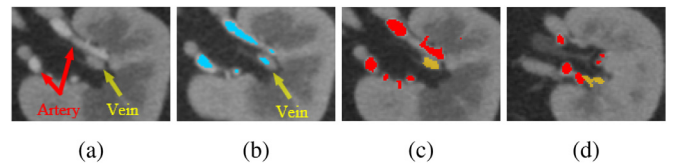


Fig. 17. One over-segmentation case: (a) one slice of original CT data; (b) initial foreground seed voxels; (c) and (d) two slices from segmentation result showing over-segmentation of renal veins marked in yellow; red regions are correctly segmented renal arteries. (For interpretation of the references to colour in this figure legend, the reader is referred to the web version of this article.)

the influence of the initial seed voxels on the segmentation results. GC's performance heavily depends on the initial seed voxels. The poorly extracted initial seeds directly lead to poor segmentation results. TC is more robust to the initial seeds. Owing to the tensor term adopted in TC, the short-boundary bias was suppressed. More tiny blood vessels were extracted by TC than GC for Case 1 (Fig. 16).

Unlike the simulated data, clinical CT data have more complex structures, such as renal veins and ureters. A simple VEF cannot easily distinguish these structures from arteries. VEF concentrates on tubular representations but ignores the vascular topological information. Our experimental results also confirmed that VEF's performances are worse on the clinical data than the simulated data, which has simple topological patterns. However, this problem can be effectively suppressed by introducing a graphical energy optimizer. Graphical energy not only considers the probabilities of all the nodes but also the smoothness between pairwise nodes. TC's over-segmentations can be controlled to an acceptable range compared to the VEF approach. As illustrated in Fig. 14, VEF suffers from severe over-segmentation of the other tubular structures; TC has fewer false positives and maintains high segmentation accuracy of tiny blood vessels. Moreover, due to the low vesselness responses at bifurcation points, VEF is weak at segmenting bifurcations. Our MRF model not only consider the Hessian-tensor term but also the intensity term. The smoothness term also helps to improve the continuity of segmentation results. Thus, our MRF model naturally address the bifurcation segmentation issue. We demonstrate one segmentation results at bifurcations in Fig. 18. As demonstrated, vesselness responses at bifurcations are lower than those of tubular structures shown in Fig. 18(a) and (b). However, our proposed TC can successfully extract bifurcations without introducing false positives.

Figs. 12 and 13 show that the TC method achieved the best and most robust segmentation performances on the clinical data. However, in some low contrast conditions, the initial terminal seeds have already over-segmented the other tubular structures. These over-segmented seeds will also be treated as prior information of the data term. The smoothness term has difficulty removing these over-segmented terminal seeds. As illustrated in Fig. 17, the over-segmented initial foreground seed voxels (s nodes) directly induced the final over-segmentation of the renal veins. Therefore, in this work, we restricted the initial seed voxels to have a high possibility of actually being blood vessels. This strategy can easily generate under-segmented initial seeds, such as Case 1 in Fig. 17, which is one reason that GC has unsatisfactory segmentation results; TC does not suffer from this problem.

Tensor-cut, which is built upon two components, intensity term and tensor term, benefits from both the GC and VEF characteristics. We introduced parameter ω to adjust the weight between the intensity and tensor terms, and λ_I and λ_T to control the weights between the data terms and smoothness terms, as shown in Eq. (11). However, this strategy causes a larger parameter search space. Compared to the GC and VEF approaches, which have only one primary parameter, tensor-cut has three parameters that must be

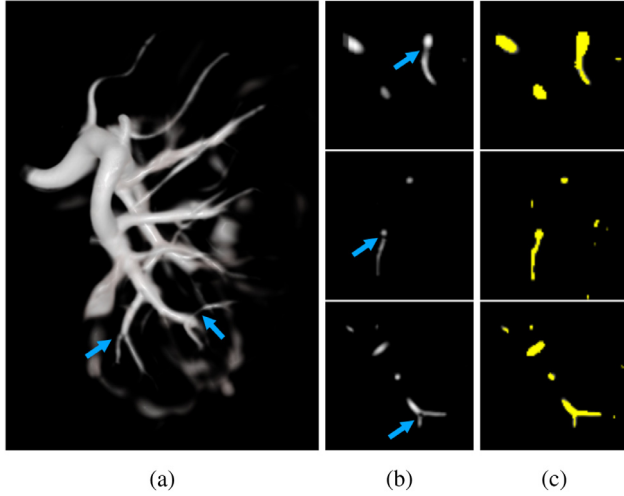


Fig. 18. Segmentation performance of bifurcations. (a) volume rendering of vesselness response calculated by VEF. (b) 2D view of VEF's response at different bifurcation points. (c) TC's segmentation results at same position.

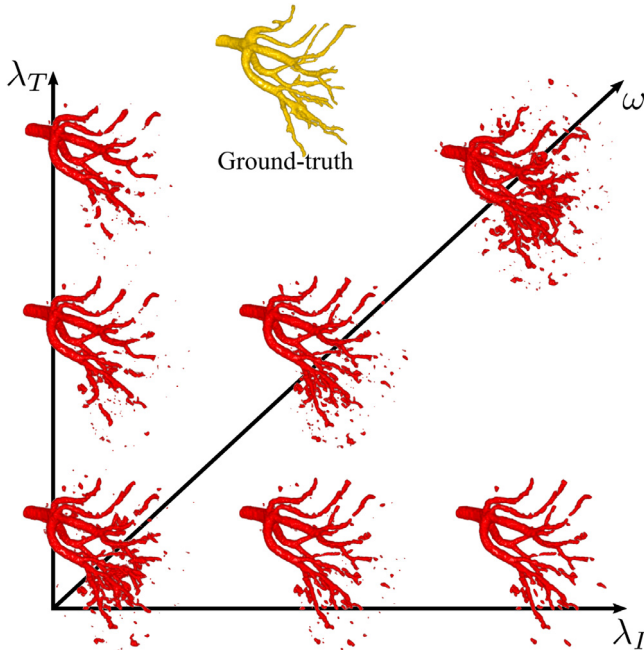


Fig. 19. Influences of parameter variations: Positive directions of three axes indicate increasing directions of three parameters.

specified. The influences of different parameters are illustrated in Fig. 19. An increasing λ_I encourages the smoothness of voxel intensity. Unlike λ_I which acts on the intensity term, an increasing λ_T mainly encourages the smoothness of vesselness. Instead of suppressing the small isolated voxels, the tubular segments are suppressed with λ_T increasing. ω controls the balance between the intensity and tensor terms, and more tubular structures can be extracted by increasing ω . Although tensor-cut has the most robust segmentation performance in the clinical experiments, simplifying its parameters remains future work.

5. Conclusion

We presented a novel unsupervised blood vessel segmentation approach using a tensor-based graph-cut method. Our simulated and clinical experiments showed that our proposed method has higher segmentation performances than other reference ap-

proaches. In this study, we focused on renal artery segmentation. Our clinical experimental results show that our tensor-cut method is robust and outperformed the other reference methods, especially on tiny blood vessels. Accurate vascular topology is the foundation of such follow-up processing as the estimation of vascular dominant regions.

Declaration of Competing Interest

The authors declare that they have no known competing financial interests or personal relationships that could have appeared to influence the work reported in this paper.

Acknowledgements

Parts of this research was supported by MEXT/JSPS KAKENHI (26108006, 26560255, 17H00867, 17K20099), and the JSPS Bilateral Collaboration Grant and AMED (191k1010036h0001)

Appendix

This section simply describes the mean and variance of Hessian tensors. The Fréchet mean generalizes the centroids to arbitrary matrix space by minimizing the Fréchet variance:

$$\bar{\mathcal{T}} = \underset{\mathcal{T} \in \mathbb{T}}{\operatorname{argmin}} \rho(\mathcal{T}), \quad (16)$$

where $\rho(\mathcal{T})$ denotes sum-of-squared distance which is defined:

$$\rho(\mathcal{T}) = \frac{1}{2N} \sum_{i=1}^N d^2(\bar{\mathcal{T}}, \mathcal{T}_i). \quad (17)$$

Geometric mean tensor $\bar{\mathcal{T}}$ is the center point on a manifold at which the Fréchet variance is minimized for any tensor $\mathcal{T} \in \mathbb{T}$. The existence and uniqueness of geometric mean has been proven by Karcher (1977). Then, Newton gradient descent solves the given minimization problem in Eq. (16). Also, the gradient of $\rho(\mathcal{T})$ is given by

$$\nabla \rho(\mathcal{T}) = -\frac{1}{N} \sum_{i=1}^N \log_{\bar{\mathcal{T}}}(\mathcal{T}_i). \quad (18)$$

Initialize $\bar{\mathcal{T}}_0$ with arbitrary tensor $\mathcal{T} \in \mathbb{T}$, and the $t + 1$ step of the Newton gradient descent procedure is given:

$$\bar{\mathcal{T}}_{t+1} = \exp_{\bar{\mathcal{T}}} \left(\frac{1}{N} \sum_{i=1}^N \log_{\bar{\mathcal{T}}_t}(\mathcal{T}_i) \right) = \bar{\mathcal{T}}_t^{\frac{1}{2}} \exp \left(\frac{1}{N} \sum_{i=1}^N \log(\bar{\mathcal{T}}_t^{-\frac{1}{2}} \mathcal{T}_i \bar{\mathcal{T}}_t^{-\frac{1}{2}}) \right) \bar{\mathcal{T}}_t^{\frac{1}{2}}. \quad (19)$$

As shown in Fig. 3, $\exp_x(\Sigma)$ is called exponential mapping, which is an inverse mapping of logarithmic mapping. Here exponential mapping is to delineates the arithmetic mean in the tangent space back to the manifold space. Gradient descent algorithm workflow is given in Algorithm 2. Detailed deduction information is available (Pennec et al., 2006).

Algorithm 2 Calculate geometric mean tensor $\bar{\mathcal{T}}$.

Input: $\mathcal{T}_i \in \mathbb{T}, (i = 1, 2, \dots, N)$

Output: Mean tensor $\bar{\mathcal{T}}$

Initialize: $\bar{\mathcal{T}}_0 = \mathcal{T}_1, t = 0, \epsilon = 0.001$

Do

$t = t + 1$ ▷ Update step

$X_t = \frac{1}{N} \sum_{k=1}^N \log_{\bar{\mathcal{T}}_t}(\mathcal{T}_k)$ ▷ Gradient

$\bar{\mathcal{T}}_{t+1} = \exp_{\bar{\mathcal{T}}_t}(X_t)$ ▷ Update mean tensor

While $\|X_t\| > \epsilon$

Since we know how to calculate the distance and the mean, the variance of tensors σ_T^2 is given:

$$\sigma_T^2 = \mathcal{E}[d^2(\bar{T}, T)] = \frac{1}{N} \sum_{i=1}^N d^2(\bar{T}, T_i), \quad (20)$$

where $\mathcal{E}[\cdot]$ is the expectation of the squared deviation from mean tensor \bar{T} . The statistics of the tensors given above, geodesic distance, geometric mean and variance, are used to compute a Gaussian mixture model (GMM) to estimate the probability distribution of the foreground and background voxels.

References

- AMIRA3-D., Analysis software for life sciences [online]. <http://www.vsg3d.com/amira>.
- Barmoutis, A., Vemuri, B.C., Shepherd, T.M., Forder, J.R., 2007. Tensor splines for interpolation and approximation of dt-mri with applications to segmentation of isolated rat hippocampi. *IEEE Trans. Med. Imaging* 26 (11), 1537–1546.
- Bauer, C., Pock, T., Sorantin, E., Bischof, H., Beichel, R., 2010. Segmentation of interwoven 3D tubular tree structures utilizing shape priors and graph cuts. *Med. Image Anal.* 14 (2), 172–184.
- Bigün, J., 1987. Optimal orientation detection of linear symmetry. In: Proceedings of the IEEE-First International Conference on Computer Vision. Linköping University Electronic Press, pp. 433–438.
- Bigün, J., Granlund, G.H., Wiklund, J., 1991. Multidimensional orientation estimation with applications to texture analysis and optical flow. *IEEE Trans. Pattern Anal. Mach. Intell.* 13 (8), 775–790.
- Boykov, Y., Veksler, O., Zabih, R., 2001. Fast approximate energy minimization via graph cuts. *IEEE Trans. Pattern Anal. Mach. Intell.* 23 (11), 1222–1239.
- Boykov, Y.Y., Jolly, M.-P., 2001. Interactive graph cuts for optimal boundary & region segmentation of objects in nd images. In: Proceedings of the Eighth IEEE International Conference on Computer Vision ICCV, 1. IEEE, pp. 105–112.
- Dempster, A.P., Laird, N.M., Rubin, D.B., 1977. Maximum likelihood from incomplete data via the em algorithm. *J. Royal Stat. Soc. Ser. B (Methodol.)* 1–38.
- Dice, L.R., 1945. Measures of the amount of ecologic association between species. *Ecology* 26 (3), 297–302.
- Esneault, S., Lafon, C., Dillenseger, J.-L., 2010. Liver vessels segmentation using a hybrid geometrical moments/graph cuts method. *IEEE Trans. Biomed. Eng.* 57 (2), 276–283.
- Fletcher, P.T., Joshi, S., 2007. Riemannian geometry for the statistical analysis of diffusion tensor data. *Signal Process.* 87 (2), 250–262.
- Fouard, C., Malandain, G., 2005. 3-D chamfer distances and norms in anisotropic grids. *Image Vis. Comput.* 23 (2), 143–158.
- Fouard, C., Malandain, G., Prohaska, S., Westerhoff, M., 2006. Blockwise processing applied to brain microvascular network study. *IEEE Trans. Med. Imaging* 25 (10), 1319–1328.
- Frangi, A.F., Niessen, W.J., Vincken, K.L., Viergever, M.A., 1998. Multiscale vessel enhancement filtering. In: Proceedings of the International Conference on Medical Image Computing and Computer-Assisted Intervention. Springer, pp. 130–137.
- Friman, O., Hindennach, M., Künnel, C., Peitgen, H.-O., 2010. Multiple hypothesis template tracking of small 3d vessel structures. *Med. Image Anal.* 14 (2), 160–171.
- Fu, H., Xu, Y., Lin, S., Wong, D.W.K., Liu, J., 2016. Deepvessel: Retinal vessel segmentation via deep learning and conditional random field. In: Proceedings of the International Conference on Medical Image Computing and Computer-Assisted Intervention. Springer, pp. 132–139.
- Gerig, G., Kubler, O., Kikinis, R., Jolesz, F.A., 1992. Nonlinear anisotropic filtering of MRI data. *IEEE Trans. Med. Imaging* 11 (2), 221–232.
- Ghosh, A., Descoteaux, M., Deriche, R., 2008. Riemannian framework for estimating symmetric positive definite 4th order diffusion tensors. In: Proceedings of the Medical Image Computing and Computer-Assisted Intervention-MICCAI 2008, pp. 858–865.
- Hamarneh, G., Jassi, P., 2010. Vascusynth: simulating vascular trees for generating volumetric image data with ground truth segmentation and tree analysis. *Computerized Medical Imaging and Graphics* 34 (8), 605–616.
- Han, S., Wang, X., 2015. Texture segmentation using graph cuts in spectral decomposition based riemannian multi-scale nonlinear structure tensor space. *Int. J. Comput. Theory Eng.* 7 (4), 259.
- Hanbay, K., Talu, M.F., 2018. A novel active contour model for medical images via the hessian matrix and eigenvalues. *Comput. Math. Appl.* 75 (9), 3081–3104.
- Jegelka, S., Bilmes, J., 2011. Submodularity beyond submodular energies: coupling edges in graph cuts. In: Proceedings of the IEEE Conference on Computer Vision and Pattern Recognition (CVPR). IEEE, pp. 1897–1904.
- Jiang, Z., Zhang, H., Wang, Y., Ko, S.-B., 2018. Retinal blood vessel segmentation using fully convolutional network with transfer learning. *Comput. Med. Imaging Graph.* 68, 1–15.
- Karcher, H., 1977. Riemannian center of mass and mollifier smoothing. *Commun. Pure Appl. Math.* 30 (5), 509–541.
- Kerkeni, A., Benabdallah, A., Manzanera, A., Bedoui, M.H., 2016. A coronary artery segmentation method based on multiscale analysis and region growing. *Comput. Med. Imaging Graph.* 48, 49–61.
- Knutsson, H., Westin, C.-F., Andersson, M., 2011. Representing local structure using tensors ii. In: Proceedings of the Scandinavian Conference on Image Analysis. Springer, pp. 545–556.
- Kohli, P., Osokin, A., Jegelka, S., 2013. A principled deep random field model for image segmentation. In: Proceedings of the IEEE Conference on Computer Vision and Pattern Recognition, pp. 1971–1978.
- Lacoste, C., Finet, G., Magnin, I.E., 2006. Coronary tree extraction from x-ray angiograms using marked point processes. In: Proceedings of the 3rd IEEE International Symposium on Biomedical Imaging: Nano to Macro. IEEE, pp. 157–160.
- Law, M.W., Chung, A.C., 2009. Efficient implementation for spherical flux computation and its application to vascular segmentation. *IEEE Trans. Image Process.* 18 (3), 596–612.
- Lesage, D., Angelini, E.D., Bloch, I., Funka-Lea, G., 2009. A review of 3D vessel lumen segmentation techniques: models, features and extraction schemes. *Med. Image Anal.* 13 (6), 819–845.
- Lin, Q., 2001. Enhancement, detection, and visualization of 3D volume data. Linköping University, Department of Electrical Engineering Ph.D. thesis.
- Lindeberg, T., 1994. Scale-space theory: a basic tool for analysing structures at different scales. *J. Appl. Stat.* 21, 224–270.
- Liskowski, P., Krawiec, K., 2016. Segmenting retinal blood vessels with deep neural networks. *IEEE Trans. Med. Imaging* 35 (11), 2369–2380.
- Lorigo, L.M., Faugeras, O.D., Grimson, W.E.L., Keriven, R., Kikinis, R., Nabavi, A., Westin, C.-F., 2001. Curves: curve evolution for vessel segmentation. *Med. Image Anal.* 5 (3), 195–206.
- Metz, C., Schaap, M., van Walsum, T., van der Giessen, A., Weustink, A., Mollet, N., Kreftin, G., Niessen, W., 2008. 3D Segmentation in the clinic: a grand challenge II—coronary artery tracking. *Insight J.* 1 (5), 6.
- Moakher, M., 2005. A differential geometric approach to the geometric mean of symmetric positive-definite matrices. *SIAM J. Matr. Anal. Appl.* 26 (3), 735–747.
- Moccia, S., Momi, E.D., Hadji, S.E., Mattos, L.S., 2018. Blood vessel segmentation algorithms - review of methods, datasets and evaluation metrics. *Comput. Methods Progr. Biomed.* 158, 71–91. <http://www.sciencedirect.com/science/article/pii/S0169260717313421>.
- Pennec, X., Fillard, P., Ayache, N., 2006. A Riemannian framework for tensor computing. *Int. J. Comput. Vis.* 66 (1), 41–66.
- Rohlfing, T., 2012. Image similarity and tissue overlaps as surrogates for image registration accuracy: widely used but unreliable. *IEEE Trans. Med. Imaging* 31 (2), 153–163.
- Rother, C., Kolmogorov, V., Blake, A., 2004. Grabcut: Interactive foreground extraction using iterated graph cuts. In: Proceedings of the ACM Transactions on Graphics (TOG), 23. ACM, pp. 309–314.
- Sato, Y., Nakajima, S., Shiraga, N., Atsumi, H., Yoshida, S., Koller, T., Gerig, G., Kikinis, R., 1998. Three-dimensional multi-scale line filter for segmentation and visualization of curvilinear structures in medical images. *Med. Image Anal.* 2 (2), 143–168.
- Schaap, M., Metz, C.T., van Walsum, T., van der Giessen, A.G., Weustink, A.C., Mollet, N.R., Bauer, C., Bogunović, H., Castro, C., Deng, X., et al., 2009. Standardized evaluation methodology and reference database for evaluating coronary artery centerline extraction algorithms. *Med. Image Anal.* 13 (5), 701–714.
- Shao, P., Qin, C., Yin, C., Meng, X., Ju, X., Li, J., Lv, Q., Zhang, W., Xu, Z., 2011. Laparoscopic partial nephrectomy with segmental renal artery clamping: technique and clinical outcomes. *Eur. Urol.* 59 (5), 849–855.
- Shao, P., Tang, L., Li, P., Xu, Y., Qin, C., Cao, Q., Ju, X., Meng, X., Lv, Q., Li, J., et al., 2012. Precise segmental renal artery clamping under the guidance of dual-source computed tomography angiography during laparoscopic partial nephrectomy. *Eur. Urol.* 62 (6), 1001–1008.
- Shikata, H., Hoffman, E.A., Sonka, M., 2004. Automated segmentation of pulmonary vascular tree from 3D CT images. In: Proceedings of the Medical Imaging Physiology, Function, and Structure from Medical Images, 5369. International Society for Optics and Photonics, pp. 107–117.
- Skibbe, H., Reisert, M., Maeda, S.-i., Koyama, M., Oba, S., Ito, K., Ishii, S., 2015. Efficient monte carlo image analysis for the location of vascular entity. *IEEE Trans. Med. Imaging* 34 (2), 628–643.
- Tang, T.W., Chung, A.C., 2007. Non-rigid image registration using graph-cuts. In: Proceedings of the International Conference on Medical Image Computing and Computer-Assisted Intervention. Springer, pp. 916–924.
- Tetteh, G., Efremov, V., Forkert, N. D., Schneider, M., Kirschke, J., Weber, B., Zimmer, C., Piraud, M., Menze, B. H., 2018. Deepvesselnet: vessel segmentation, centerline prediction, and bifurcation detection in 3-D angiographic volumes. arXiv:1803.09340.
- Tyrrell, J.A., di Tommaso, E., Fujia, D., Tong, R., Kozak, K., Jain, R.K., Roysam, B., 2007. Robust 3-D modeling of vasculature imagery using superellipsoids. *IEEE Trans. Med. Imaging* 26 (2), 223–237.
- Vasilevskiy, A., Siddiqi, K., 2002. Flux maximizing geometric flows. *IEEE Trans. Pattern Anal. Mach. Intell.* 24 (12), 1565–1578.
- Vicente, S., Kolmogorov, V., Rother, C., 2008. Graph cut based image segmentation with connectivity priors. In: Proceedings of the IEEE Conference on Computer vision and pattern recognition, 2008. CVPR 2008. IEEE, pp. 1–8.
- Wang, C., Kagajo, M., Nakamura, Y., Oda, M., Yoshino, Y., Yamamoto, T., Mori, K., 2016a. Precise renal artery segmentation for estimation of renal vascular dominant regions. In: Proceedings of the SPIE Medical Imaging. International Society for Optics and Photonics, 97842M–97842M.
- Wang, C., Oda, M., Hayashi, Y., Yoshino, Y., Yamamoto, T., Frangi, A.F., Mori, K., 2016b. Tensor-based graph-cut in Riemannian metric space and its application to renal artery segmentation. In: Proceedings of the International Conference on Medical Image Computing and Computer-Assisted Intervention. Springer, pp. 353–361.

- Wang, Y., Chen, W., Yu, T., Zhang, Y., 2010. Hessian based image structure adaptive gradient vector flow for parametric active contours. In: Proceedings of the IEEE International Conference on Image Processing. IEEE, pp. 649–652.
- Wink, O., Niessen, W.J., Viergever, M.A., 2004. Multiscale vessel tracking. *IEEE Trans. Med. Imaging* 23 (1), 130–133.
- Wörz, S., Rohr, K., 2008. Cramér-rao bounds for estimating the position and width of 3D tubular structures and analysis of thin structures with application to vascular images. *J. Math. Imaging Vis* 30 (2), 167–180.
- Yoshino, Y., Yamamoto, T., Funahashi, Y., Oda, M., Kagajo, M., Wang, C., Mori, K., Gotoh, M., 2015. Computational analysis of recovery from ischemic damage to kidney function undergoing robotic partial nephrectomy for renal tumor. *Suppl. J. Endourol.* 916–924.
- Zhu, X., Xue, Z., Gao, X., Zhu, Y., Wong, S.T., 2009. Voles: Vascularity-oriented level set algorithm for pulmonary vessel segmentation in image guided intervention therapy. In: Proceedings of the IEEE International Symposium on Biomedical Imaging: From Nano to Macro, ISBI'09. IEEE, pp. 1247–1250.